Space Weather

RESEARCH ARTICLE
10.1029/2019SW002246

Improving Predictions of High-Latitude Coronal Mass Ejections Throughout the Heliosphere

C. Scolini[1,2], E. Chané[1], J. Pomoell[3], L. Rodriguez[2], and S. Poedts[1,4]

[1]Centre for mathematical Plasma Astrophysics, Department of Mathematics, KU Leuven, Leuven, Belgium, [2]Solar-Terrestrial Centre of Excellence — SIDC, Royal Observatory of Belgium, Brussels, Belgium, [3]Department of Physics, University of Helsinki, Helsinki, Finland, [4]Institute of Physics, University of Maria Curie-Skłodowska, Lublin, Poland

Key Points:
- We use the EUHFORIA heliospheric model to investigate the modeling of high-latitude cone CMEs
- We find that commonly used low-latitude approximations fail in reproducing the initial shape of high-latitude cone CMEs
- If not corrected, such approximations may affect predictions at locations of high latitude and close-to-the-Sun space missions

Correspondence to:
C. Scolini,
camilla.scolini@kuleuven.be

Citation:
Scolini, C., Chané, E., Pomoell, J., Rodriguez, L., & Poedts, S. (2020). Improving predictions of high-latitude coronal mass ejections throughout the heliosphere. *Space Weather*, *18*, e2019SW002246. https://doi.org/10.1029/2019SW002246

Received 14 MAY 2019
Accepted 17 FEB 2020
Accepted article online 19 FEB 2020

Abstract Predictions of the impact of coronal mass ejections (CMEs) in the heliosphere mostly rely on cone CME models, whose performances are optimized for locations in the ecliptic plane and at 1 AU (e.g., at Earth). Progresses in the exploration of the inner heliosphere, however, advocate the need to assess their performances at both higher latitudes and smaller heliocentric distances. In this work, we perform 3-D magnetohydrodynamics simulations of artificial cone CMEs using the EUropean Heliospheric FORecasting Information Asset (EUHFORIA), investigating the performances of cone models in the case of CMEs launched at high latitudes. We compare results obtained initializing CMEs using a commonly applied approximated (Euclidean) distance relation and using a proper (great circle) distance relation. Results show that initializing high-latitude CMEs using the Euclidean approximation results in a teardrop-shaped CME cross section at the model inner boundary that fails in reproducing the initial shape of high-latitude cone CMEs as a circular cross section. Modeling errors arising from the use of an inappropriate distance relation at the inner boundary eventually propagate to the heliospheric domain. Errors are most prominent in simulations of high-latitude CMEs and at the location of spacecraft at high latitudes and/or small distances from the Sun, with locations impacted by the CME flanks being the most error sensitive. This work shows that the low-latitude approximations commonly employed in cone models, if not corrected, may significantly affect CME predictions at various locations compatible with the orbit of space missions such as Parker Solar Probe, Ulysses, and Solar Orbiter.

1. Introduction

Coronal mass ejections (CMEs) are large-scale eruptions of plasma and magnetic fields from the Sun considered to be the main source of intense space weather disturbances at Earth (Gosling, 1993; Koskinen & Huttunen, 2006). When impacting our planet, they can directly or indirectly affect a variety of human activities, including industry sectors, infrastructures, and services (Schrijver et al., 2015), as well as military operations (Knipp et al., 2018). In order to predict such events and to enable mitigation, the international community has devoted efforts toward the development of models capable of providing reliable predictions of CME impacts (time and extent) at Earth.

Over the past decades, a plethora of CME models has been developed for operational and research purposes (see, e.g., Riley et al., 2018). Among them, physics-based heliospheric models that describe CMEs by means of so-called cone models have gained an important position in space weather operations, due to their relative simplicity of use and robustness (e.g., the ENLIL model, Odstrčil et al., 2004). In cone models, CMEs are described as hydrodynamic plasma clouds characterized by a spherical self-similarly expanding geometry, that is, having a constant angular width, propagation direction, and speed (Xie et al., 2004). Although the lack of an internal magnetic structure in the ejected plasma makes cone models incapable of providing reliable predictions of the CME magnetic field at Earth or other locations in space, such models have been (and are) successfully used to predict the hit (yes/no) and arrival time of CME-driven shocks at various locations in space (Guo et al., 2018; Mays et al., 2015; Palmerio et al., 2019).

Despite the extensive use of cone models for both research and forecasting purposes, a lack of rigorous definitions has led to significant confusion in the terminology used to define specific CME characteristics such as their global shape. In a recent work, Scolini et al. (2018) investigated the notion of "spherical" CME

©2020. The Authors.
This is an open access article under the terms of the Creative Commons Attribution License, which permits use, distribution and reproduction in any medium, provided the original work is properly cited.

shape in cone models, pointing out how the concept of spherical CME can be interpreted in various ways depending on the details used to initalize it in simulations via time-dependent inner boundary conditions. In particular, these authors tested various possible alternative implementation approaches using the EUropean Heliospheric FORecasting Information Asset heliospheric model (EUHFORIA, Pomoell & Poedts, 2018). In their study, Scolini et al. (2018) focused on CMEs launched in the direction of the Earth, that is, in the ecliptic plane, finding that details in the definition of the CME shape can significantly influence in situ CME predictions of several parameters, such as the estimated CME arrival time and shock parameters at 1 AU, and CME geoeffectiveness predictions (such as predictions of the K_p index and magnetopause stand-off distance). For the first time, these authors also suggested that such CME initialization details would affect particularly CMEs launched at high latitudes. Such class of CMEs, although making up only a small fraction of the totality of CMEs observed, has been previously studied by multiple authors (Cremades et al., 2006; Gopalswamy et al., 2003, 2015), who reported hundreds of high-latitude CMEs during Solar Cycles 23 and 24, typically associated with the eruptions of polar filaments.

At the same time, forecasting efforts have traditionally focused on CME predictions at Earth (notable exceptions are the early works by Odstrčil & Pizzo, 1999; Reisenfeld et al., 2003), and the forecasting performances of current models have been fine-tuned on the near-Earth space, that is, at a heliocentric distance of 1 AU and close to the ecliptic plane. However, as the attention of the community turns to the study of new environments in the solar system (see, e.g., Guo et al., 2018; Palmerio et al., 2019; Riley et al., 2019), investigating how the approximations used in current CME models affect predictions at different locations than Earth has become a critical issue to address in order to expand our prediction horizon, in particular toward higher latitudes and lower heliocentric distances.

In this work, we compare the prediction performance of the cone CME model implemented in EUHFORIA in the case of CMEs launched in and outside of the solar equatorial plane. The purpose is that of assessing for the first time how approximations employed in the CME intialization/insertion phase affect the CME global shape and evolution in the heliosphere, and consequently in situ predictions along the orbit of various space missions throughout the heliosphere, depending on the initial latitudinal direction of the CME.

The paper is structured as follows: section 2 contains a description of the EUHFORIA model and a discussion of the various cone CME implementations employed in this study. In section 3 we describe the model setup and the artificial CME event used as test case in simulations aimed at quantifying the effects of details in the CME shape initialization, on predictions at different locations in the heliosphere. In section 4 we present the results obtained and compare the predictions for CMEs launched in and outside of the solar equatorial plane. In section 5 we discuss the results and present our conclusions.

2. The EUHFORIA Model

EUHFORIA is a recently developed 3-D magnetohydrodynamics (MHD) heliospheric model designed for space weather research and prediction purposes (Pomoell & Poedts, 2018). The model is composed of a coronal part, whose domain extends from the photosphere or low corona up to 0.1 AU, and a heliospheric part usually covering the heliocentric distances between 0.1 and 2 AU (i.e., the inner heliosphere).

The coronal part consists of a semiempirical Wang-Sheeley-Arge-like (WSA-like; Arge et al., 2004) model, which provides the solar wind conditions at the inner boundary of the heliospheric domain based on synoptic maps of the photospheric magnetic field from the Global Oscillation Network Group (GONG) network. In the low corona, below the source surface radius (corresponding to the coronal height at which the magnetic field is set to be purely radial), the WSA model computes the magnetic field via a Potential Field Source Surface (Altschuler & Newkirk, 1969) model. The source surface radius is here kept to a default value of 2.6 solar radii as in Pomoell and Poedts (2018). In the upper corona (between an "interface radius" here set at 2.3 solar radii, and 0.1 AU), the magnetic field lines are extended by a Schatten Current Sheet (Schatten et al., 1969) model in a nearly radial fashion. A detailed analysis of the effect of the source surface radius and interface radius heights on modeling results in the corona can be found in Asvestari et al. (2019).

Given the 3-D coronal magnetic field topology determined by the models above, the solar wind speed at 0.1 AU is derived as function of the magnetic field properties: $v_{sw} = v_{sw}(f, d)$, which depends on the flux tube expansion factor (f), and the distance of the foot point of the flux tube to the nearest coronal hole boundary (d), as determined by the previously mentioned models (see equations (1) and (2) in Pomoell & Poedts, 2018).

The functional form $v_{sw}(f, d)$ used in EUHFORIA is the same as the one given by McGregor et al. (2011) (equation (2) therein, regarded as the original WSA model), with the exception of the parameter w that normalizes the dependence of the solar wind speed on the distance to the nearest coronal hole boundary.

The other solar wind parameters at 0.1 AU (i.e., the solar wind temperature T_{sw} and number density N_{sw}) are recovered based on v_{sw} by imposing a constant kinetic energy density and a constant plasma thermal pressure at the coronal outer boundary (i.e., at 1 AU). In this work we employ the same formulas and the same parameters as described by Pomoell and Poedts (2018). A first assessment of the performance of the EUHFORIA solar wind modeling at 1 AU, using the same set of parameters employed here, can be found in Hinterreiter et al. (2019).

The solar wind map generated by the coronal model is then used as inner boundary condition for the heliospheric model, which solves 3-D time-dependent ideal MHD equations in a computational domain extending from 0.1 to 2 AU in the radial direction (r), and spanning $\pm$ 60° in latitude (θ), and $\pm$ 180° in longitude (ϕ). Throughout this paper, all coordinates are given in the Heliocentric Earth Equatorial coordinate system.

In addition to the solar wind background, EUHFORIA allows to model CMEs in the heliosphere by inserting them in the heliospheric domain via time-dependent boundary conditions at the inner heliospheric boundary, that is, at 0.1 AU. In the cone model, CMEs are assumed to be characterized by a (quasi-)spherical shape and are initialized using the following five input parameters that are required to univocally determine their time-dependent cross section at the inner boundary: the insertion start time t_{CME}, speed v_{CME}, latitude θ_{CME}, longitude ϕ_{CME}, and half width $\omega_{CME}/2$. These parameters are normally derived from remote sensing white-light observations of CMEs in the corona. In addition, due to more limited observational inputs, two additional parameters defining the CME mass density and temperature are set to be homogeneous and equal to the following default (average) values: $\rho_{CME} = 1 \cdot 10^{-18}$ kg m^{-3} and $T_{CME} = 0.8 \cdot 10^{6}$ K (Pomoell & Poedts, 2018). As discussed by Scolini et al. (2018), the determination of the CME global shape in the model also depends on three extra parameters: the angular width-radius relation, the opening angle time profile, and the distance relation at the heliospheric inner boundary. The latter parameter, in particular, has been identified as the one having the largest impact on the determination of the shape of CMEs launched outside of the solar equatorial plane.

The default cone model configuration in EUHFORIA and other similar models (e.g., ENLIL) is such that a cone CME is advected through the $r = 0.1$ AU boundary using an Euclidean (simplified) distance relation. In other words, the distance of a point p from the CME center of propagation on the spherical shell constituting the inner boundary is calculated as

$$d_{pl} = \sqrt{(\theta_p - \theta_{CME})^2 + (\phi_p - \phi_{CME})^2}, \tag{1}$$

where $(\phi_p - \phi_{CME})$ and $(\theta_p - \theta_{CME})$ are the longitudinal and latitudinal angles between the point p and the CME propagation vector. If, at a given time t, d_{pl} is small enough to fall within the CME opening angle $\theta(t)$, the point p is considered to be part of the CME and the plasma properties of the solar wind at that location (speed, mass density, temperature, etc.) are replaced by the plasma properties of the CME. Scolini et al. (2018) pointed out that equation (1) is inappropriate for defining the distance between two points on the model heliospheric inner boundary; that is, it is inconsistent with its spherical nature, and the following more accurate great-circle distance relation should be preferred:

$$d_{sph} = \arccos(\cos\theta_p \cos\theta_{CME} \cos(\phi_p - \phi_{CME}) + \sin\theta_p \sin\theta_{CME}). \tag{2}$$

To visualize the difference between these two distance relations, in Figure 1 we show a comparison between the distance contour levels at the inner boundary obtained using equations (1) and 2, for a CME launched from the solar equator ($\theta_{CME} = 0°$, $\phi_{CME} = 0°$) and for one at high latitude ($\theta_{CME} = 40°$, $\phi_{CME} = 0°$). As shown in the left panel of Figure 1, the simplified equation (1) provides a good approximation in the case of CMEs launched near the solar equator, where the deviation between the resulting contours is small but visible. On the other hand, this deviation becomes much more significant for CMEs launched away from the solar equator (right panel of Figure 1). A quantification of their difference is provided by the relative (percentage) error metric:

$$\epsilon_d = \frac{d_{pl} - d_{sph}}{d_{sph}} \cdot 100. \tag{3}$$

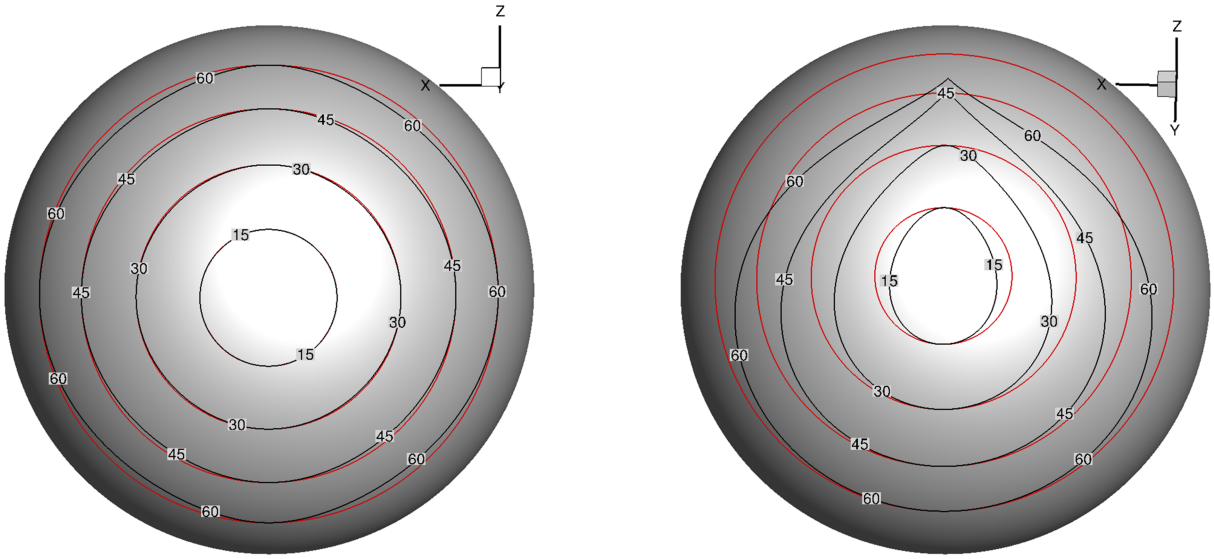

Figure 1. CME cross section at the heliospheric inner boundary for CMEs of different half widths, launched at two different latitudes. The contour levels for the distance computed by equation (1) are marked in black, while those from equation (2) are in red. The view is such that the observer is along the axis normal to the heliospheric inner boundary and passing through the CME center. (left) CME launched at $\theta_{\mathrm{CME}} = 0°$, $\phi_{\mathrm{CME}} = 0°$. (right) CME launched at $\theta_{\mathrm{CME}} = 40°$, $\phi_{\mathrm{CME}} = 0°$.

Figure 2 shows a contour map of ϵ_d in the longitude-latitude 2-D plane, for the two different CME insertion directions considered. Assuming a typical CME half width <45°, the error remains below 4% in all directions if the CME is launched from the solar disk center (Figure 2, left); that is, the use of equation (1) provides a good approximation of a circle in such cases, as θ_p remains relatively small. As the majority of CMEs is launched at relatively low latitudes, and CME models are generally validated for predictions in or close to the ecliptic plane, where CME impacts are most geoeffective, this error has not been previously noted nor quantified. However, the distance error reaches 40% in the case of a CME launched at $\theta_{\mathrm{CME}} = 40°$, $\phi_{\mathrm{CME}} = 0°$ (Figure 2, right). This can be understood by considering that at higher latitudes, meridians converge toward the poles, hence $(\phi_p - \phi_{\mathrm{CME}})^2$ in equation (1) progressively becomes an increasingly worse approximation of the longitudinal distance between a point p and the axis of propagation. This result demonstrates that the approximated distance relation used in cone models results in a significant deformation of the intended spherical CME cross section, leading to a CME shape that is inconsistent with the assumption of spherical CMEs which is at the basis of cone models. This effect, passed mostly unnoticed in previous studies, is affecting most prominently the global shape of CMEs propagating outside of the solar equatorial plane,

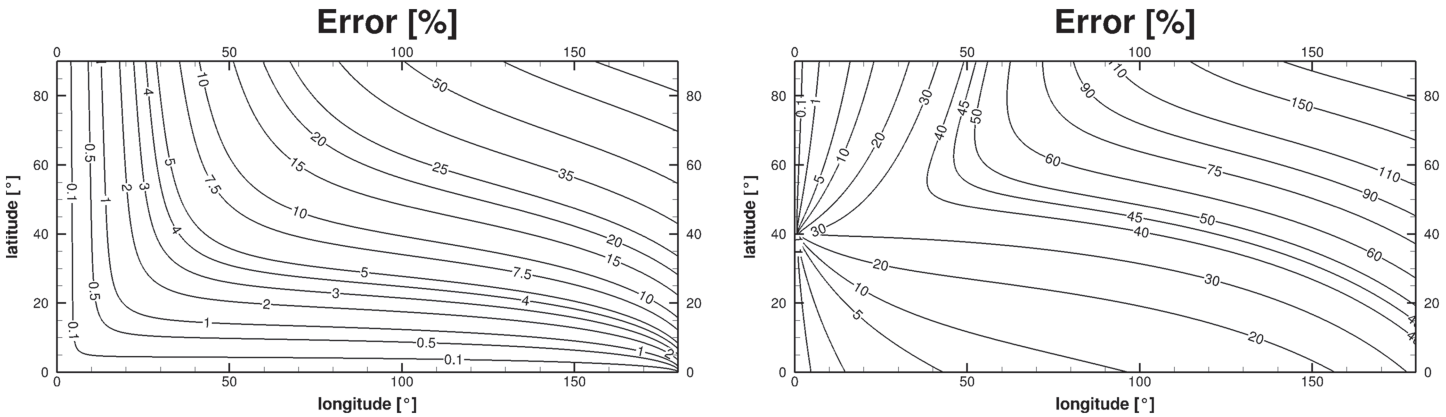

Figure 2. Contour map of the relative (percentage) error ϵ_d (equation (3)) affecting the initialization of the CME cross section at the heliospheric inner boundary, for the two different CME directions considered, as function of the Heliocentric Earth Equatorial latitude (θ) and longitude (ϕ). (left) CME launched at $\theta_{\mathrm{CME}} = 0°$, $\phi_{\mathrm{CME}} = 0°$. (right) CME launched at $\theta_{\mathrm{CME}} = 40°$, $\phi_{\mathrm{CME}} = 0°$.

Table 1
Summary of the CME Input Parameters Used in the Four Simulations Performed, Labeled According to the Naming Convention Used in this Work

Run	Distance relation	θ_{CME}	ϕ_{CME}	$\omega_{CME}/2$	v_{CME}
01a	equation (1)	0°	0°	45°	850 km s^{-1}
01b	equation (2)	0°	0°	45°	850 km s^{-1}
02a	equation (1)	40°	0°	45°	850 km s^{-1}
02b	equation (2)	40°	0°	45°	850 km s^{-1}

suggesting this relation may also impact space weather predictions at high-latitude locations such as along the orbits of major past and future solar missions (e.g., Ulysses, Solar Orbiter).

3. Test Case Event: An Artificial CME on 6 June 2008

To investigate the effect of the inner boundary distance relation on heliospheric CME simulations performed with EUHFORIA, we use a similar approach as in Scolini et al. (2018). As test case event, we simulate a hypothetical CME (no CMEs were observed during the considered time period) that erupted from the solar central meridian on 6 June 2008 at 00:00 UT. As discussed by Scolini et al. (2018), the selection of the specific period was carried out in order to ensure quiet solar wind conditions in the Earth's ecliptic quadrant (Temmer et al., 2011), in order to minimize the effects of deformation of the CME structure as consequence of the interaction with winds of different characteristics. The choice of a realistic solar wind background as opposed to a synthetic solar wind description was made in order to have a more realistic environment for the CME to propagate. As input for the semiempirical coronal model we use the GONG standard synoptic standard map generated on 6 June 2008 at 02:04 UT, that is, close to the CME insertion time (https://gong.nso.edu/data/magmap/QR/bqs/200806/mrbqs080606/mrbqs080606t0204c2071_349.fits.gz).

We perform a total of four simulations, consisting of two pairs: in the first pair, the CMEs are launched from the solar equator (Runs 01a and 01b), while in the second pair the CMEs are launched at 40° above the solar equatorial plane (Runs 02a and 02b). The naming conventions “XXa” and “XXb” indicate the use of equations (1) (Euclidean geometry) and 2 (spherical geometry) as distance relations, respectively. A summary of the simulations, including the CME input parameters used, is presented in Table 1.

In this work, we use a uniform grid in all directions, with 512 cells in the radial direction (corresponding to a radial resolution of $\Delta r \simeq 0.0037$ AU) and a 2° angular resolution in the latitudinal and longitudinal directions. We have chosen this resolution in order to test the model in an operational framework, that is, using a resolution similar to that used for daily runs at prediction centers. Compared to default values, here the latitudinal domain has been extended to ±80° in order to allow the investigation of the CME shape initialization close to the poles. All simulations are performed using EUHFORIA version 1.0.4.

4. Results and Discussion

4.1. Heliospheric Inner Boundary

Figure 3 shows the radial speed v_r on the EUHFORIA heliospheric inner boundary ($r = 0.1$ AU) during the CME insertion period, for each of the four simulations performed, from three different points of view. The area where the CME is being inserted ($v_r = 850$ km s^{-1}) is visible as the red (high-speed) patch. The CME cross sections extracted from Runs 01a and 01b appear quite similar, and are both characterized by a (quasi-)circular shape. On the other hand, when launched at high latitudes, CMEs initialized using equation (1) appear quite deformed in their cross section, exhibiting a teardrop shape that significantly differs from the intended circular cross section.

An alternative representation of the radial speed at the EUHFORIA heliospheric inner boundary during the CME insertion is provided in Figure 4. Here, the longitudinal and (co-)latitudinal coordinates are projected in 2-D using a cylindrical (equirectangular) projection. In this visualization format, the CME cross sections in Runs 01a and 01b (Figure 3, top and second rows, respectively) retain their apparent circular shape, while the teardrop shape appearing in the third row of Figure 3 is transformed into a circular shape after projection on the 2-D plane. On the other hand, the circular cross section characterizing a truly spherical CME in 3-D simulations (Figure 3, bottom row) appears deformed asymmetrically at high latitudes when

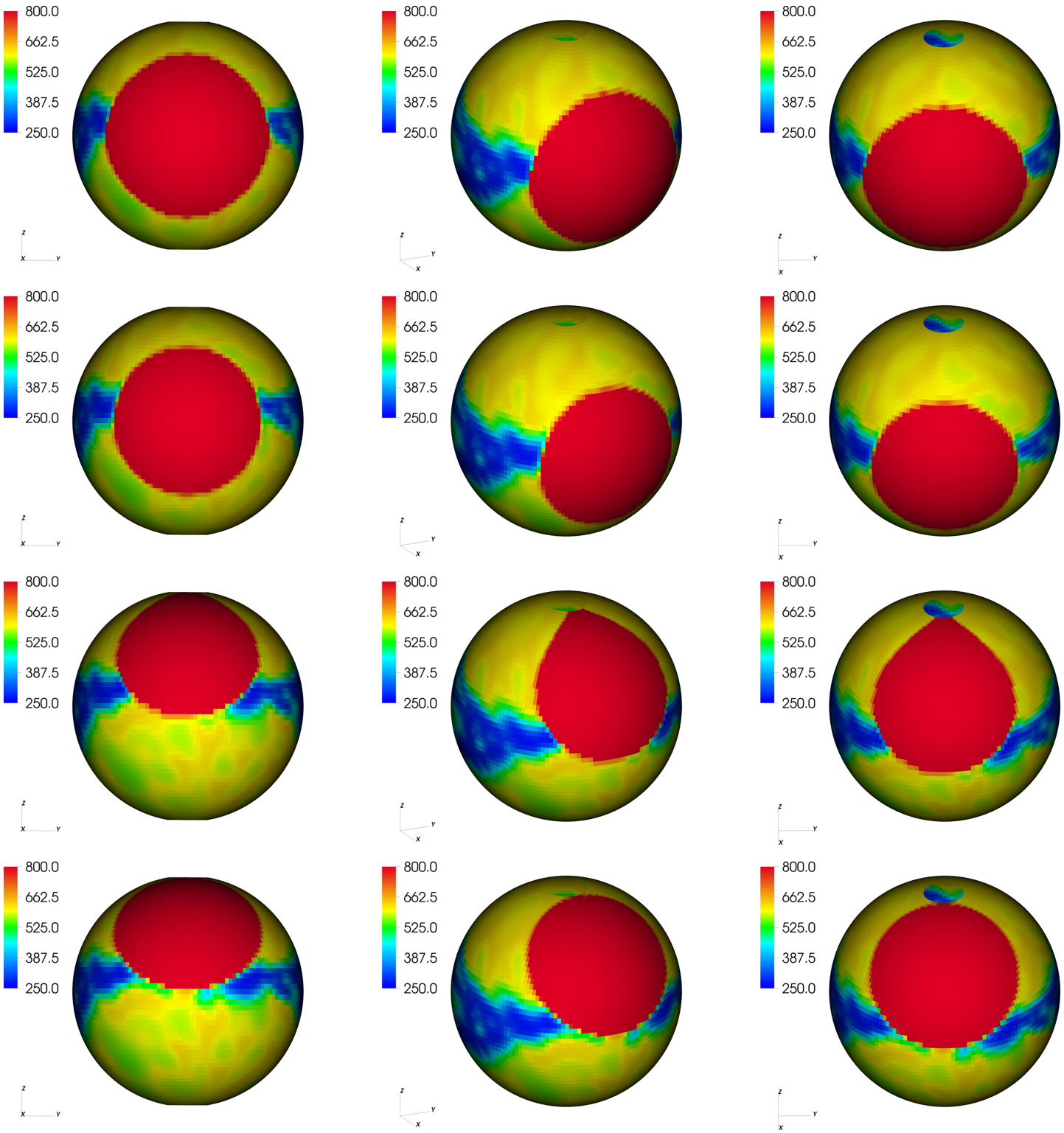

Figure 3. 3-D views of the radial velocity (v_r, in units of km s^{-1}) at the heliospheric inner boundary on 6 June 2008 at 04:00 UT, for the four simulations performed. (top row) Run 01a, Euclidean distance relation, $\theta_{\mathrm{CME}} = 0°$, $\phi_{\mathrm{CME}} = 0°$. (second row) Run 01b, great-circle distance relation, $\theta_{\mathrm{CME}} = 0°$, $\phi_{\mathrm{CME}} = 0°$. (third row) Run 02a, Euclidean distance relation, $\theta_{\mathrm{CME}} = 40°$, $\phi_{\mathrm{CME}} = 0°$. (bottom row) Run 02b, great-circle distance relation, $\theta_{\mathrm{CME}} = 40°$, $\phi_{\mathrm{CME}} = 0°$. Each column provides a different point of view. The area where the CME is being inserted ($v_r = 850$ km s^{-1}) is visible as the red (high-speed) patch.

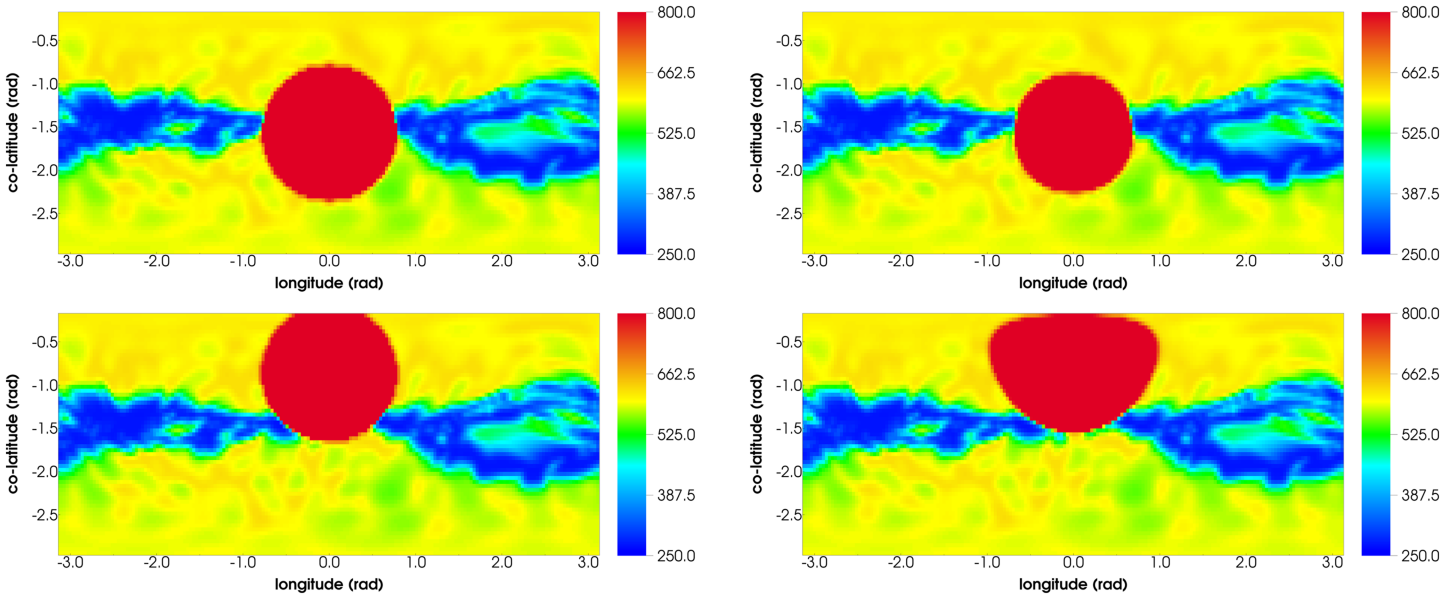

Figure 4. Projected 2-D view of the radial velocity (v_r, in units of km s^{-1}) at the heliospheric inner boundary on 6 June 2008 at 04:00 UT, for the four simulations performed. (top left) Run 01a, Euclidean distance relation, $\theta_{\mathrm{CME}} = 0°$, $\phi_{\mathrm{CME}} = 0°$. (top right) Run 01b, great-circle distance relation, $\theta_{\mathrm{CME}} = 0°$, $\phi_{\mathrm{CME}} = 0°$. (bottom left) Run 02a, Euclidean distance relation, $\theta_{\mathrm{CME}} = 40°$, $\phi_{\mathrm{CME}} = 0°$. (bottom right) Run 02b, great-circle distance relation, $\theta_{\mathrm{CME}} = 40°$, $\phi_{\mathrm{CME}} = 0°$. The area where the CME is being inserted ($v_r = 850$ km s^{-1}) is visible as the red (high-speed) patch.

projected in 2-D. This 2-D visualization of the CME during its insertion in the heliosphere is widely used in the community; for example, an equirectangular 2-D projection of the model inner boundary is provided as default model output for ENLIL runs at the Community Coordinated Modeling Centre. In this regard, we note that extra care should be used when interpreting this kind of data products, as the projection in 2-D could lead to a misleading interpretation of the actual CME shape modeled in simulations. When a CME launched at high latitudes appears characterized by a circular cross section in a plot similar to the one in Figure 4 (bottom right), this implies that the simulated CME is actually characterized by a noncircular teardrop-shaped cross section on the spherical inner boundary surface, that is, in actual 3-D space, which is not the intention for a cone CME.

4.2. Heliospheric Propagation

To establish the relevance of the aforementioned modeling error to space weather applications and CME predictions in the heliosphere, we further investigate its evolution in the heliospheric domain by comparing simulations employing different distance relations. To investigate in which regions of the heliospheric domain the error arising from the use of the approximated distance relation (equation (1)) is higher, we subtract point-by-point the radial velocity values (v_r) in Runs XXb with that in Runs XXa at a given time. In Figure 5 we show the results of this process for the two simulation pairs. We have marked the regions where the difference ($\Delta v_r = v_r^{XXb} - v_r^{XXa}$) is larger by red and blue contour surfaces. As clearly visible, differences in the CME shapes not only exist at the heliospheric inner boundary, but they are maintained after the CME is completely inserted in the heliosphere. These differences are confined around the CME flanks, and comparing the level of contour surfaces at different latitudes, we see that they are strongest in the case of CMEs launched outside of the solar equatorial plane. Moreover, the differences are more intense (i.e., higher levels and more extended contours) close to the Sun, and they tend to fade out while the CME propagates outward, reasonably because of its interaction with the background solar wind.

To quantify the extent of these differences, we measure their latitudinal span in 3-D simulation output taken on 7 June 2008 at 20:00 UT, when the CME front has reached approximately 1 AU. We perform a 2-D cut of the heliospheric domain at $\phi = 0°$ and we there consider the region in the r-θ plane where the difference in radial velocity Δv_r between Runs 01a and 01b is larger than 24 km/s (corresponding to the most transparent red contour surface in the bottom left panel of Figure 5). We find that this region spans ~33° in latitude, from ~17° to ~50° in the Northern Hemisphere (a similar situation is expected in the Southern Hemisphere based on symmetry reasons). For a CME characterized by a 45° half width such as the one modeled here

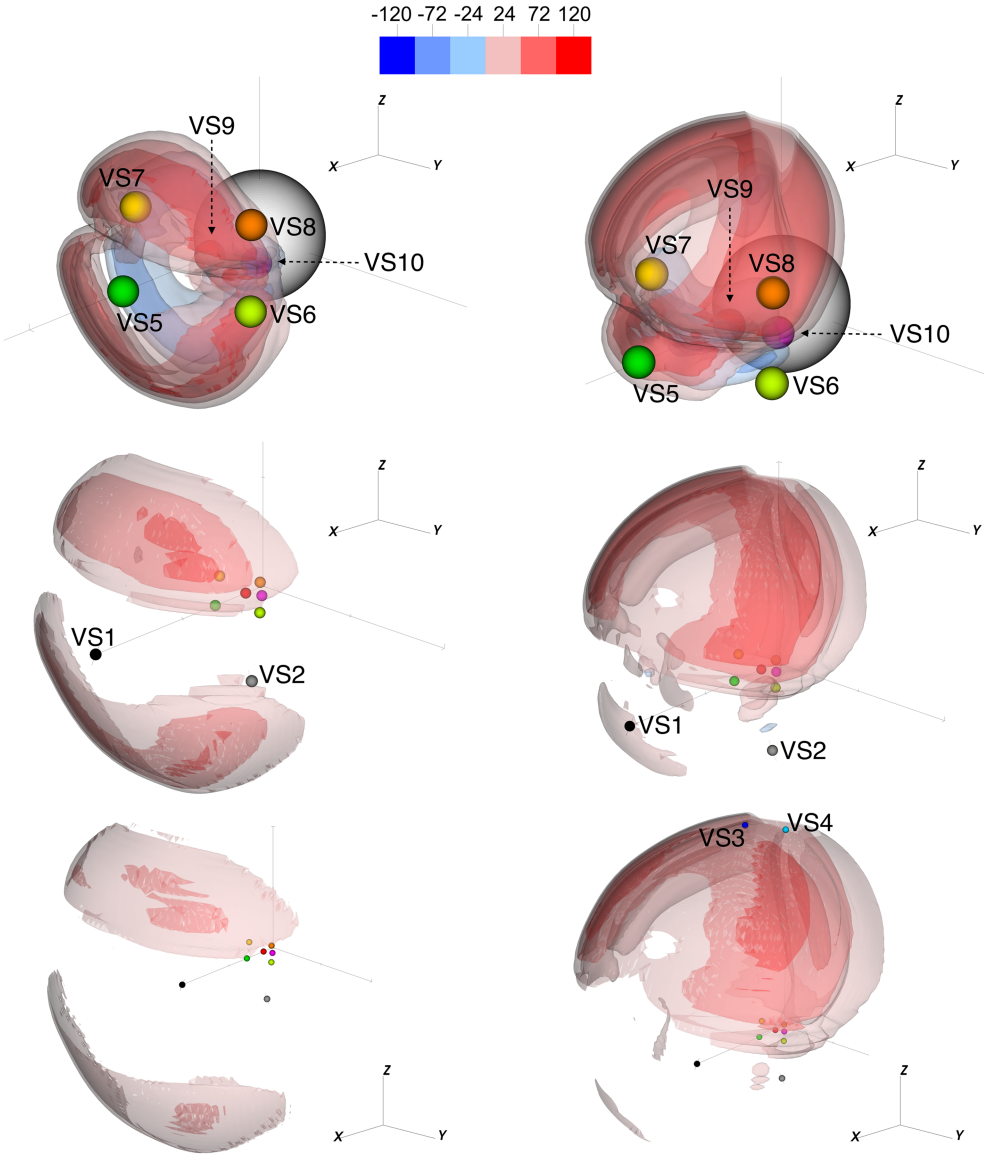

Figure 5. 3-D contour plots showing the difference in radial velocity (Δv_r, in units of km s^{-1}) between run pairs, at three different times in the simulations: 6 June at 10:00 UT (top), 7 June at 20:00 UT (center), 9 June at 12:00 UT (bottom). (left column: Runs 01x ($\theta_{CME} = 0°$, $\phi_{CME} = 0°$). (right column) Runs 02x ($\theta_{CME} = 40°$, $\phi_{CME} = 0°$). The positions of virtual spacecraft ("VSx"), chosen according to the typical radial and latitudinal location of notable spacecraft in the heliosphere, are marked by the colored spheres and labeled according to Table 2. The distance of the observer from the Sun is changing in order to follow the CME front in space and time.

(as the CME heliospheric propagation is characterized by a quasi-self-similar behavior), the latitudinal extent of the radial speed difference $\Delta v_r \geq 24$ km/s accounts for more than half of the CME latitudinal span. For the higher threshold $\Delta v_r \geq 72$ km/s (corresponding to the intermediate red contour surface in the bottom left panel of Figure 5), we find that the region spans ~22° in latitude, from ~22° to ~44° in the Northern Hemisphere. In other words, the error introduced by the use of an improper distance relation affects a significant portion of the CME front.

4.3. Implications for CME Predictions

Cone CME models are widely employed in the community both as supporting tools for observational studies on CME propagation, and as operational space weather forecasting tools because of their robustness and simplicity to use. In both cases, (yes/no) predictions of the hit or miss of a CME at given spacecraft and planetary locations represent the most basic prediction output considered. Establishing the relevance of the

Table 2
Location of Virtual spacecraft, Labeled According to the Naming Convention Used in This Work

Virtual spacecraft	r_{vs}	θ_{vs}	ϕ_{vs}	Representative orbit
VS1, VS2	1.0 AU	0°	0° , 40°	Earth/L1
VS3, VS4	1.8 AU	75°	0° , 40°	Ulysses
VS5, VS6	0.3 AU	0°	0° , 40°	Mercury/MESSENGER
VS7, VS8	0.3 AU	25°	0° , 40°	Solar Orbiter
VS9, VS10	0.11 AU	0°	0° , 40°	Parker Solar Probe

Note. The radial and latitudinal position of virtual spacecraft locations have been chosen so to be consistent with notable orbits (mentioned in Column 5).

distance relation modeling error to hit/miss CME predictions is therefore critical to advance our understanding of the sources of errors involved in space weather predictions, and particularly those associated to the assumptions made on the CME shape and geometry at the heliospheric inner boundary.

Previous works assessed that the reliability of hit/miss predictions using cone CME models is limited on one side by observational uncertainties affecting the reconstruction of the CME input parameters (direction and geometry) from coronal observations (Guo et al., 2018; Palmerio et al., 2019), and on the other side by the oversimplification of the CME shape generally assumed when initializing CMEs in heliospheric models (Mays et al., 2015). Observational errors on the reconstruction of the CME half width, longitude, and latitude are estimated to be of the order of 10° (Rodriguez et al., 2011; Thernisien et al., 2009), and considering them alone, their cumulative effects generate a "buffer zone" as wide as ∼30°, where any of the two CME prediction outcomes (hit or miss, in this case) is equally acceptable as compatible with observational uncertainties. If not correctly accounted for, the fact that CMEs are often characterized by elongated and tilted ellipsoidal shapes instead of spherical ones further contributes to enlarge this buffer zone significantly (Mays et al., 2015).

In addition to these two sources of uncertainty related to the CME modeling, in this work we identify the existence of a third source of errors, arising from the use of an approximated distance relation at the model inner boundary, which can contribute to an erroneous prediction of the CME hit or miss in the case of glancing encounters with high-latitude CMEs. The differences between runs employing different distance relations in Figure 5 provided evidence of how predictions of hits/misses in the case of glancing encounters with high-latitude CMEs can be affected by the distance relations used in the CME initialization phase in a buffer zone as wide as ∼20°. As a result, we suggest that the buffer zone for predictions of CME hits/misses in the case of glancing CME encounters should be estimated to be larger than expected in previous studies, due to a previously unidentified contributing term associated to the use of an improper distance relation in the CME initialization at the heliospheric inner boundary. Although the ultimate assessment of the distance relation effects on predictions should involve (1) the testing of a statistical number of real CME events, as well as (2) the consideration of errors occurring in the modeling of the solar wind background, we here speculate that the substitution of equation (1) with equation (2) may be significantly beneficial for studies investigating the hit or miss of glancing CMEs, as it would allow to reduce the uncertainty by a term compatible with observational uncertainties (∼20° compared to ∼30°).

We also note that in this work we have only modeled a single CME (although representative of an average event) propagating through a single (realistic, quiet) ambient solar wind. Although we have no theoretical arguments to suppose that a different ambient solar wind would change significantly the global features of the modeling error recovered in this work, we leave for future study the investigation of its exact dependence on the characteristics of the ambient solar wind.

In order to provide the community with a more complete set of guidelines on the relevance of this CME shape modeling error to space weather predictions, we further consider in situ predictions at various locations in the heliosphere. To visualize the effect of the modeling errors resulting from the use of equation (1) on in situ plasma properties, we place virtual (i.e., artificial) spacecraft at selected locations in the heliosphere. The latitudinal (θ_{vs}) and radial (r_{vs}) coordinates of each spacecraft are set at latitudes and radial distances consistent with the orbits of relevant past, present, and future space missions, as listed in Table 2. To make sure to

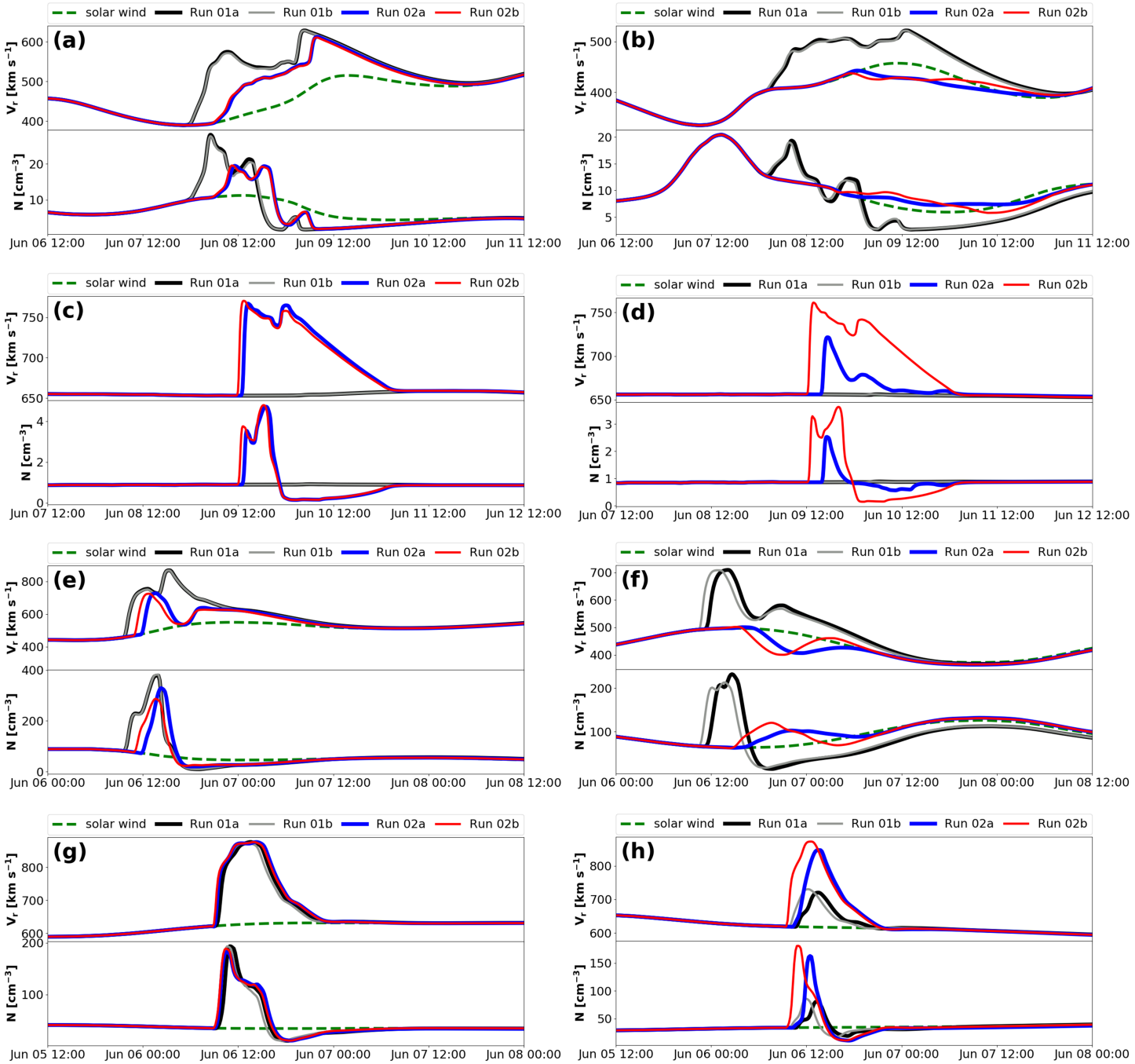

Figure 6. In situ radial speed and number density time series from the four simulations at the various virtual spacecraft considered. (a) VS1. (b) VS2. (c) VS3. (d) VS4. (e) VS5. (f) VS6. (g) VS7. (h) VS8. The results from Run 01a are shown as continuous black lines, those from Run 01b are shown as continuous gray lines, those from Run 02a are shown as continuous blue lines, and those from Run 02b are shown as continuous red lines. The dashed green lines correspond to the unperturbed background solar wind.

cover, for each simulation, locations impacted by the CME center as well as locations impacted by the CME flanks, we place virtual spacecraft pairs at $\phi_{vs} = 0°$ and $\phi_{vs} = 40°$ in longitude, that is, that are separated by 40° in longitude. Figure 6 shows the results from the four runs (black, gray, blue, and red continuous lines for Runs 01a, 01b, 02a, and 02b, respectively) at selected virtual spacecraft locations (VS1–VS8), together with the pristine background solar wind results (dashed green line) obtained by running an additional simulation where no CME was inserted. As visible from Figures 6a and 6b, results at locations consistent with the position of the Earth (VS1/VS2) appear largely independent of the particular distance relation used to

define the CME cross section at the heliospheric inner boundary. On the other hand, at higher latitudes and radial distances compatible with the position of Ulysses during polar passages (VS3/VS4, Figures 6c and 6d), in situ predictions appear significantly affected by the distance relation chosen, both in terms of the CME arrival time as well as in the solar wind radial speed and density profiles, particularly in the case of a CME impact from the flank (Runs 02x at VS4). On the solar equatorial plane, at locations compatible with the orbit of Mercury/MESSENGER (VS5/VS6, Figures 6e and 6f), that is, closer to the Sun than Earth, in situ predictions of the CME arrival time appear more affected by the distance relation used when the spacecraft are impacted from the flank (Runs 01x and 02x at VS5, Runs 02x at VS6). VS7/VS8 are located at the same heliocentric distance as VS5/VS6, but at an inclination of 25° above the solar equatorial plane. At this distance and latitude, compatible with the orbit of the future Solar Orbiter mission, we observe a situation similar to VS3/VS4, with similar predictions for all runs at VS7 (CME impact close to the center, Figure 6g), and significant variation among the predictions at VS8 due to a CME flank encounter at high latitudes (Figure 6h). At locations very close to the heliospheric inner boundary and compatible with the orbit of Parker Solar Probe (VS9/VS10), we report the presence of modeling artifacts indicating that CMEs cannot be reliably simulated below 0.2 AU using the initiation scheme starting at 0.1 AU in its current form. A more detailed investigation of boundary-related effects on predictions close to the Sun is left for future studies. Finally, we note that spacecraft located more than 45° away from the CME direction of propagation (VS3/VS4 in Runs 01x, VS2/VS6/VS10 in Runs 02x) are not impacted by the CME, whose initial half width is set to 45°. This is, such virtual spacecraft are located too far away from the CME direction of propagation to be directly impacted. At these spacecraft locations, fluctuations (and particularly drops) of the in situ parameters with respect to the quiet solar wind conditions (green dashed line) are interpreted as perturbations resulting from the passage of the CME in nearby space, but not as associated to the CME itself.

5. Conclusions

In this paper we have discussed the initialization of cone CMEs in 3-D MHD heliospheric models and its consequences on modeling results and space weather predictions outside of the ecliptic plane. Despite the widespread use of such models for space weather research and forecasting purposes, very few investigations on the effects CME shape initialization details have on CME predictions in the heliosphere were carried out in the past years. The work expands on a previous study (Scolini et al., 2018) that first investigated multiple parameters entering the initialization of cone CMEs in the EUHFORIA heliospheric model, suggesting that CME predictions far from the ecliptic plane would be significantly affected by details in the definition of the CME shape such as the distance relation employed during the CME insertion phase. In the present work, we have therefore extended this analysis by simulating an artificial CME launched outside of the solar equatorial (and ecliptic) plane. After having discussed the limitations of the approximated (Euclidean geometry) distance relation currently used in most cone CME models (equation (1)), and after having presented an easy-to-implement alternative that removes the errors at high latitudes (equation (2), that is, the great-circle distance relation consistent with the inner boundary spherical geometry), we have performed heliospheric simulations of an artificial CME launched from the solar central meridian on 6 June 2008. The input parameters for the simulated CME event were chosen in order to be representative of an average CME, and the CME was first launched on the solar equatorial plane (i.e., close to the ecliptic plane), and then at a latitude of 40° north. Each simulation was performed using both the distance relations discussed, for a total of four simulations (two pairs). Modeling results were compared to theoretical expectations. The impact of the distance relation on in situ predictions was also discussed by comparing the speed and density results obtained from different simulations at various locations in space. The main results of our work can be summarized as follows.

1. From analytical calculations, at the heliospheric inner boundary the error from the use of an approximated distance relation is expected to increase with the CME width and to be maximal in the high-latitude portion of the CME (Figures 1 and 2). The error is expected to be larger for CMEs launched far from the ecliptic plane, where relative errors on the identification of the CME border can reach 40% for typical CME widths. In the case of CMEs launched close to the ecliptic plane, errors are generally lower than 4%.
2. EUHFORIA simulation output provide full 3-D information on the inserted CME shape and its evolution in the heliosphere. As visible in Figure 3, for CMEs launched far from the ecliptic plane, the use of an approximated distance relation generates a teardrop-shaped CME cross section instead of a spherical one

at the heliospheric inner boundary. The difference between the two cross sections is particularly visible at high-latitude CME flanks, as already expected from analytical derivations. This is also reflected in the 3-D speed distribution of the CME after its insertion in the heliospheric domain (Figure 5, right column). Although more limited, similar results are also found for low-latitude CMEs (Figure 5, left column), in which case the use of the approximated distance relation affects the modeling of the CME flanks in a region as wide as ∼33° in latitude for a CME of typical half width. Based on these results, we speculate that the use of equation (1) can affect the prediction of CME hits or misses near the CME flanks in a region as wide as ∼20°. The width of this "buffer zone" may therefore be comparable to the typical uncertainties introduced by observational limitations, and as such, distance relation effects should be considered as a contributing source of uncertainty in future space weather prediction studies.

3. Employing an approximated (i.e., Euclidean geometry) distance relation in the CME initialization affects the prediction of in situ CME parameters at a variety of locations, particularly when considering CMEs launched far from the ecliptic plane (CME teardrop shape effects) impacting spacecraft located at high latitudes and/or low distances from the Sun (such as Ulysses, Parker Solar Probe, and Solar Orbiter). In general, predictions at virtual spacecraft located away from the CME direction of propagation, that is, spacecraft hit by the CME flanks, are more sensitive to the CME shape initialization details than spacecraft located near or along it (CME flank effects). Particular care is therefore needed when considering spacecraft orbiting near the poles, where we observe a cumulative result of the teardrop shape and the CME flank effects (e.g., at VS4).

This work has shown how the approximated distance relation employed in most 3-D MHD heliospheric simulations of cone CMEs significantly alters modeling results and space weather predictions at high latitudes in the heliosphere. This modeling error can be completely removed via a simple substitution of the approximated relation, with an exact relation that accounts for the spherical nature of the heliospheric inner boundary in the model. If not corrected, this error can potentially affect in situ CME predictions at spacecraft orbiting very close to the Sun (e.g., Parker Solar Probe) and/or characterized by highly inclined orbits (e.g., the Ulysses mission and the upcoming Solar Orbiter). Although more prominent in the case of high-latitude CMEs, this modeling error also affects low-latitude CMEs, which constitute the majority of the CMEs observed. Furthermore, the relative CME-spacecraft angular separation has also been identified as important factor, with higher prediction variabilities at spacecraft hit by CME flanks. Although high-latitude CMEs are actually not extremely rare events, the so-far limited time spent by spacecraft at high latitudes makes the search for a real CME/ICME case study so far very challenging. Nevertheless, in the light of the recent and future launch of new missions exploring the heliosphere at low radial distances and high latitudes (e.g., Parker Solar Probe and Solar Orbiter), and of the increased attention to solar wind and CME predictions at a variety of locations in space (see, e.g., Guo et al., 2018; Riley et al., 2019; Palmerio et al., 2019), results from this work are expected to become even more significant in the future. They will provide significant insights on the prediction performances of widely used CME models, with the aim of helping the progress of space weather predictions at Earth and more "exotic" locations in the heliosphere.

Acknowledgments

C. S. and E. C. were funded by the Research Foundation-Flanders (FWO) (grant Nos. 1S42817N and 12M0119N). J. P. acknowledges funding from the University of Helsinki 3-year grant project 490162 and the SolMAG project (4100103) funded by the European Research Council (ERC) in the framework of the Horizon 2020 Research and Innovation Programme. EUHFORIA is developed as a joint effort between the University of Helsinki and KU Leuven. The full validation of solar wind and CME modeling is being performed within the CCSOM project (http://www.sidc.be/ccsom/). The EUHFORIA website, including a repository for simulation results and the possibility for users to access the code, is currently under construction; please contact the authors for model details. The full 3-D simulation output and 1-D time series discussed in this paper are archived online in the Harvard Dataverse and can be retrieved from the following link (https://doi.org/10.7910/DVN/J9LFG0 (Scolini, 2019)). These results were obtained in the framework of the projects C14/19/089 (KU Leuven), G.0A23.16N (FWO), and C 90347 (ESA Prodex). The simulations were carried out at the VSC–Flemish Supercomputer Center, funded by the Hercules foundation and the Flemish Government–Department EWI. The authors thank the Editor Noé Lugaz and the anonymous referees for their help in reviewing the manuscript.

References

Altschuler, M. D., & Newkirk, G. (1969). Magnetic fields and the structure of the solar corona. I: Methods of calculating coronal fields. *Solar Physics*, *9*(1), 131–149. https://doi.org/10.1007/BF00145734

Arge, C. N., Luhmann, J. G., Odstrčil, D., Schrijver, C. J., & Li, Y. (2004). Stream structure and coronal sources of the solar wind during the May 12th, 1997 CME. *Journal of Atmospheric and Solar-Terrestrial Physics*, *66*, 1295–1309. https://doi.org/10.1016/j.jastp.2004.03.018

Asvestari, E., Heinemann, S. G., Temmer, M., Pomoell, J., Kilpua, E., Magdalenić, J., & Poedts, S. (2019). Reconstructing coronal hole areas with EUHFORIA and adapted WSA model: optimizing the model parameters. *Journal of Geophysical Research: Space Physical*, *124*, 8280–8297. https://doi.org/10.1029/2019JA027173

Cremades, H., Bothmer, V., & Tripathi, D. (2006). Properties of structured coronal mass ejections in solar cycle 23. *Advances in Space Research*, *38*(3), 461–465. https://doi.org/10.1016/j.asr.2005.01.095

Gopalswamy, N., Shimojo, M., Lu, W., Yashiro, S., Shibasaki, K., & Howard, R. A. (2003). Prominence eruptions and coronal mass ejection: A Statistical study using microwave observations. *The Astrophysical Journal Letters*, *586*(1), 562–578. https://doi.org/10.1086/367614

Gopalswamy, N., Yashiro, S., & Akiyama, S. (2015). Kinematic and energetic properties of the 2012 March 12 polar coronal mass ejection. *The Astrophysical Journal Letters*, *809*(1), 106. https://doi.org/10.1088/0004-637X/809/1/106

Gosling, J. T. (1993). The solar flare myth. *Journal of Geophysical Research*, *98*, 18,937–18,950. https://doi.org/10.1029/93JA01896

Guo, J., Dumbović, M., Wimmer-Schweingruber, R. F., Temmer, M., Lohf, H., Wang, Y., & Posner, A. (2018). Modeling the evolution and propagation of 10 September 2017 CMEs and SEPs arriving at Mars constrained by remote sensing and in situ measurement. *Space Weather*, *16*, 1156–1169. https://doi.org/10.1029/2018SW001973

Hinterreiter, J., Magdalenić, J., Temmer, M., Verbeke, C., Jebaraj, I. C., Samara, E., & Isavnin, A. (2019). Assessing the performance of EUHFORIA modeling the background solar wind. *Solar Physics*, *294*(12), 170. https://doi.org/10.1007/s11207-019-1558-8

Knipp, D. J., Fraser, B. J., Shea, M. A., & Smart, D. F. (2018). On the little-known consequences of the 4 August 1972 ultra-fast coronal mass ejecta: Facts, commentary, and call to action. *Space Weather*, *16*(11), 1635–1643. https://doi.org/10.1029/2018SW002024

Koskinen, H. E. J., & Huttunen, K. E. J. (2006). Geoeffectivity of coronal mass ejections. *Space Science Reviews*, *124*, 169–181. https://doi.org/10.1007/s11214-006-9103-0

Mays, M. L., Thompson, B. J., Jian, L. K., Colaninno, R. C., Odstrčil, D., Möstl, C., & Zheng, Y. (2015). Propagation of the 7 January 2014 CME and resulting geomagnetic non-event. *The Astrophysical Journal Letters*, *812*, 145. https://doi.org/10.1088/0004-637X/812/2/145

McGregor, S. L., Hughes, W. J., Arge, C. N., Odstrčil, D., & Schwadron, N. A. (2011). The radial evolution of solar wind speeds. *Journal of Geophysical Research*, *116*, A03106. https://doi.org/10.1029/2010JA016006

Odstrčil, D., & Pizzo, V. J. (1999). Three-dimensional propagation of coronal mass ejections in a structured solar wind flow 2. CME launched adjacent to the streamer belt. *Journal of Geophysical Research*, *104*(A1), 493–504. https://doi.org/10.1029/1998JA900038

Odstrcil, D., Riley, P., & Zhao, X. P. (2004). Numerical simulation of the 12 May 1997 interplanetary CME event. *Journal of Geophysical Research*, *109*, A02116. https://doi.org/10.1029/2003JA010135

Palmerio, E., Scolini, C., Barnes, D., Magdalenić, J., West, M. J., Zhukov, A. N., et al. (2019). Multipoint study of successive coronal mass ejections driving moderate disturbances at 1 AU. *The Astrophysical Journal Letters*, *878*(1), 37. https://doi.org/10.3847/1538-4357/ab1850

Pomoell, J., & Poedts, S. (2018). EUHFORIA: European heliospheric forecasting information asset. *Journal of Space Weather and Space Climate*, *8*, A35. https://doi.org/10.1051/swsc/2018020

Reisenfeld, D. B., Gosling, J. T., Forsyth, R. J., Riley, P., & St. Cyr, O. C. (2003). Properties of high-latitude CME-driven disturbances during Ulysses second northern polar passage. *Geophysical Research Letters*, *30*(19), 8031. https://doi.org/10.1029/2003GL017155

Riley, P., Downs, C., Linker, J. A., Mikić, Z., Lionello, R., & Caplan, R. M. (2019). Predicting the structure of the solar corona and inner heliosphere during Parker Solar Probe's first perihelion pass. *The Astrophysical Journal Letters*, *874*(2), L15. https://doi.org/10.3847/2041-8213/ab0ec3

Riley, P., Mays, M. L., Andries, J., Amerstorfer, T., Biesecker, D., Delouille, V., & Zhao, X. (2018). Forecasting the arrival time of coronal mass ejections: Analysis of the CCMC CME scoreboard. *Space Weather*, *16*, 1245–1260. https://doi.org/10.1029/2018SW001962

Rodriguez, L., Mierla, M., Zhukov, A. N., West, M., & Kilpua, E. (2011). Linking remote-sensing and in situ observations of coronal mass ejections using STEREO. *Solar Physics*, *270*(2), 561–573. https://doi.org/10.1007/s11207-011-9784-8

Schatten, K. H., Wilcox, J. M., & Ness, N. F. (1969). A model of interplanetary and coronal magnetic fields. *Solar Physics*, *6*(3), 442–455. https://doi.org/10.1007/BF00146478

Schrijver, C. J., Kauristie, K., Aylward, A. D., Denardini, C. M., Gibson, S. E., Glover, A., & Vilmer, N. (2015). Understanding space weather to shield society: A global road map for 2015-2025 commissioned by COSPAR and ILWS. *Advances in Space Research*, *55*, 2745–2807. https://doi.org/10.1016/j.asr.2015.03.023

Scolini, C. (2019). EUHFORIA-high-latitude-cone-CMEs. Harvard Dataverse, https://doi.org/10.7910/DVN/J9LFG0

Scolini, C., Verbeke, C., Poedts, S., Chané, E., Pomoell, J., & Zuccarello, F. P. (2018). Effect of the initial shape of coronal mass ejections on 3-D MHD simulations and geoeffectiveness predictions. *Space Weather*, *16*, 754–771. https://doi.org/10.1029/2018SW001806

Temmer, M., Rollett, T., Möstl, C., Veronig, A. M., Vršnak, B., & Odstrčil, D. (2011). Influence of the ambient solar wind flow on the propagation behavior of interplanetary coronal mass ejections. *The Astrophysical Journal Letters*, *743*, 101. https://doi.org/10.1088/0004-637X/743/2/101

Thernisien, A., Vourlidas, A., & Howard, R. A. (2009). Forward modeling of coronal mass ejections using STEREO/SECCHI data. *Solar Physics*, *256*(1-2), 111–130. https://doi.org/10.1007/s11207-009-9346-5

Xie, H., Ofman, L., & Lawrence, G. (2004). Cone model for halo CMEs: Application to space weather forecasting. *Journal of Geophysical Research*, *109*, A03109. https://doi.org/10.1029/2003JA010226